

## Are the TRACE-P measurements representative of the western Pacific during March 2001?

Juno Hsu,<sup>1</sup> Michael J. Prather,<sup>1</sup> Oliver Wild,<sup>2</sup> Jostein K. Sundet,<sup>3</sup> Ivar S. A. Isaksen,<sup>3</sup> Edward V. Browell,<sup>4</sup> Melody A. Avery,<sup>4</sup> and Glen W. Sachse<sup>4</sup>

Received 23 July 2003; revised 29 October 2003; accepted 25 November 2003; published 31 January 2004.

[1] Observations of CO and O<sub>3</sub> from the Transport and Chemical Evolution over the Pacific (TRACE-P) campaign are compared with modeled distributions from the FRSGC/UCI CTM driven by the Oslo T63L40 ECMWF forecast meteorology. The model-measurement comparison is made within the context of how well the TRACE-P observations represent the springtime chemistry and ozone distributions over eastern Asia and the western Pacific in March 2001 and uses the four-dimensional (4-D) extended domain from the model to provide unbiased statistics. A key question is whether the limited sampling density or mission strategy led to a statistically biased sample. To address this question, we examine a diverse range of statistical analyses of the observations of CO and O<sub>3</sub>. The middle percentiles of the cumulative probability functions for CO in the free troposphere are representative (and reproduced by the CTM), but those in the boundary layer are not. The frequency of low-CO, stratospheric influence is well matched along flight tracks but is atypical of the extended domain. The percentiles of the latitude-by-height distribution of lidar O<sub>3</sub> show how the CTM reproduces the nonrepresentative clumpy nature of the observations but has too low a tropopause about the jet region (30–35N). Adaptive kernel estimation of the 2-D probability density of O<sub>3</sub>-CO correlations shows a very good simulation of two different chemical regimes (stratospheric and polluted) that is quite different from the extended domain but also highlights the failure to predict CO > 400 ppb. Empirical orthogonal function analysis of the O<sub>3</sub> vertical profiles shows how six EOFs can effectively describe the 4-D structures of O<sub>3</sub> over this entire domain. The latitude-by-longitude maps of the principal components provide an excellent test of the CTM simulation along flight tracks and clearly show the unique sampling of O<sub>3</sub> events by the TRACE-P flights. In many cases the ability of the model to simulate the nonrepresentative observations implies a clear skill in matching the unique meteorological and chemical features of the region. **INDEX TERMS:** 0322 Atmospheric Composition and Structure: Constituent sources and sinks; 0365 Atmospheric Composition and Structure: Troposphere—composition and chemistry; 0368 Atmospheric Composition and Structure: Troposphere—constituent transport and chemistry; **KEYWORDS:** TRACE-P measurements, CTM simulations, representativeness, sampling bias, ozone and CO<sub>2</sub> comparisons, EOF, PDFs

**Citation:** Hsu, J., M. J. Prather, O. Wild, J. K. Sundet, I. S. A. Isaksen, E. V. Browell, M. A. Avery, and G. W. Sachse (2004), Are the TRACE-P measurements representative of the western Pacific during March 2001?, *J. Geophys. Res.*, 109, D02314, doi:10.1029/2003JD004002.

### 1. Introduction

[2] In trying to understand atmospheric composition on a global scale, instantaneous measurements of trace gases made at specific sites are often assumed to be representative of a larger region over a longer period. For example, the

NOAA CMDL flask network [Dlugokencky *et al.*, 1994; Conway *et al.*, 1994] has provided the global mean latitudinal gradient as well as trends on the total atmospheric burdens of CH<sub>4</sub> and CO<sub>2</sub>, based solely on biweekly sampling at a number of remote sites. The assumption that these limited, surface measurements can be used to integrate the total atmospheric burden is necessary but far-reaching. In other cases, many single-location, surface, or sonde measurement programs have argued that their data are representative of the entire boundary layer [e.g., Haszpra, 1999; Inoue and Masueda, 2001] or the free troposphere for a greater region [e.g., Navasquez and Rus, 1991; Gallardo *et al.*, 2000]. Compared with these examples, recent airborne regional campaigns have provided an extremely dense,

<sup>1</sup>Earth System Science, University of California, Irvine, Irvine, California, USA.

<sup>2</sup>Frontier Research System for Global Change, Yokohama, Japan.

<sup>3</sup>Department of Geophysics, University of Oslo, Oslo, Norway.

<sup>4</sup>NASA Langley Research Center, Hampton, Virginia, USA.

latitudinal, longitudinal, and vertical sampling over several weeks (e.g., TRACE-P, PEM, NARE, CEPEX, MINOS). These data sets provide extensive statistics on the atmospheric chemistry of the region and thus are often assumed to be fully representative of the location and period. Nevertheless, even such high-density campaign data are greatly undersampled compared with atmospheric variability, and, further, the design of campaigns to study specific processes may result in statistically biased sampling of the region. For example, the NASA Transport and Chemical Evolution over the Pacific (TRACE-P) measurement campaign [Jacob *et al.*, 2003] had the primary goal of studying the export of pollution from eastern Asia. Understanding the representativeness of these campaign data would greatly strengthen their use in global studies.

[3] In addition, understanding of the representativeness of a given set of observations can help evaluate the accuracy of model simulations of those observations. Matching the observed statistics when the observations are representative of the sampling region is one measure of skill; however, if the observations are a statistically biased sampling, then accurate model simulation implies a clear skill in matching the unique meteorological and chemical features of the region. In the case when there is representative sampling from a campaign, the discrepancy between the flight-track observations and the model simulation cannot be dismissed as meteorological error and is more likely due to a fundamental or systematic error in the model such as emission levels, chemistry, or large-scale spatial gradients. In the case of statistically biased sampling, the mismatch between observations and model can perhaps be attributed to errors in the modeled meteorological fields, such as the height of convective outflows or the timing of frontal passing. Here we evaluate the accuracy of our global chemistry-transport model (CTM) simulations of the TRACE-P observations of CO and O<sub>3</sub> within the context of how these measurements are representative of the western Pacific during March 2001.

[4] For TRACE-P the community developed several, independent, high-resolution four-dimensional (4-D) CTM simulations for that region and period that do a commendable job on matching many of the measurements [e.g., Kiley *et al.*, 2003; Wild *et al.*, 2003; Carmichael *et al.*, 2003; Pierce *et al.*, 2003; Liu *et al.*, 2003; C. Mari *et al.*, The effect of clean warm conveyor belts on the export of pollution from East Asia, submitted to *Journal of Geophysical Research*, 2004, hereinafter referred to as Mari *et al.*, submitted manuscript, 2004]. Here we use the FRSGC/UCI/Oslo chemistry-transport model (T63L40 resolution with EC forecast fields) to generate a densely sampled 4-D data set for each chemical species for the TRACE-P region. The accuracy of our CTM simulations is determined by comparing a wide range of statistical features of O<sub>3</sub> (in situ and lidar) and CO (in situ) from (1) the observations and (2) the CTM simulations along flight tracks. The representativeness of the TRACE-P sampling is determined by parallel comparisons between (2) the CTM flight-track data and (3) the CTM simulations over the extended 4-D domain (i.e., the eastern Asia-western Pacific region for the month of frequent flight measurements).

[5] A first approach in comparing such TRACE-P species measurements with model simulations is to plot the two overlapping time series for each flight. From parallel

measurement-model plots of several species one can visually identify the temporal and spatial scales of variability and also the correlation of different species. Another, more quantitative method plots the modeled versus measured abundances as a scatter plot, yielding a measure of the accuracy of the simulation through a linear regression (for CO from TRACE-P, see Figure 1 in the work of Kiley *et al.* [2003]). Here we resort to a new range of statistical methods that allow us to compare not only the measurements with the model at the specific measurement locations but also the model sampled along flight tracks versus an extended 4-D domain.

[6] Section 2 describes the FRSGC/UCI version of the CTM and our simulations of the extended TRACE-P domain. In addition, two statistical techniques used in this study are described: the adaptive kernel estimation for construction of 2-D Probability Density Functions (PDFs) to characterize the O<sub>3</sub>-CO correlations and Empirical Orthogonal Functions (EOFs) for analysis of vertical structures in the lidar O<sub>3</sub> profiles. Cumulative probability distributions for in situ CO, in situ O<sub>3</sub>, and lidar O<sub>3</sub> are examined in section 3. Latitude-height sections of the O<sub>3</sub> abundance from the lidar sampling are shown for the 10th, 50th, and 90th percentiles of both observation and model in section 4. The same CTM statistics are also presented for the extended TRACE-P domain rather than just the flight tracks. In section 5 the O<sub>3</sub>-CO correlations observed along the flight tracks are compared with the model for individual flights. These data are combined into a single, two-dimensional probability distribution for all flights to compare with CTM simulation of both the flight tracks and the extended TRACE-P domain. In section 6, EOFs are used to describe the vertical features of the O<sub>3</sub> distribution and to show where these features are prevalent off the coast of Asia. Conclusions regarding the accuracy of the CTM simulation of TRACE-P observations in relation to the representativeness of the observing strategy are given in section 7.

## 2. Methodology

### 2.1. Chemical Transport Model

[7] The chemical fields used in this study are generated by the Frontier Research System for Global Change (FRSGC) version of the University of California, Irvine (UCI) global chemical transport model (CTM), described by Wild and Prather [2000]. The model is run at T63 resolution ( $1.9^\circ \times 1.9^\circ$ ), with 37  $\sigma$ -levels in the vertical and is driven by 3-hour averaged meteorological fields for Spring 2001 generated with the European Centre for Medium-Range Weather Forecasts (ECMWF) Integrated Forecast System (IFS). The configuration of the model and the meteorological data used for the TRACE-P period are described by Wild *et al.* [2003]. The model simulates the tropospheric production of ozone during the TRACE-P period reasonably well, with notable exceptions in the polluted boundary layer, where production is overestimated, and in the upper free troposphere, where it may be underestimated [Wild *et al.*, 2003]. In addition, a linearized chemistry is used for stratospheric ozone [McLinden *et al.*, 2000], and in combination with the

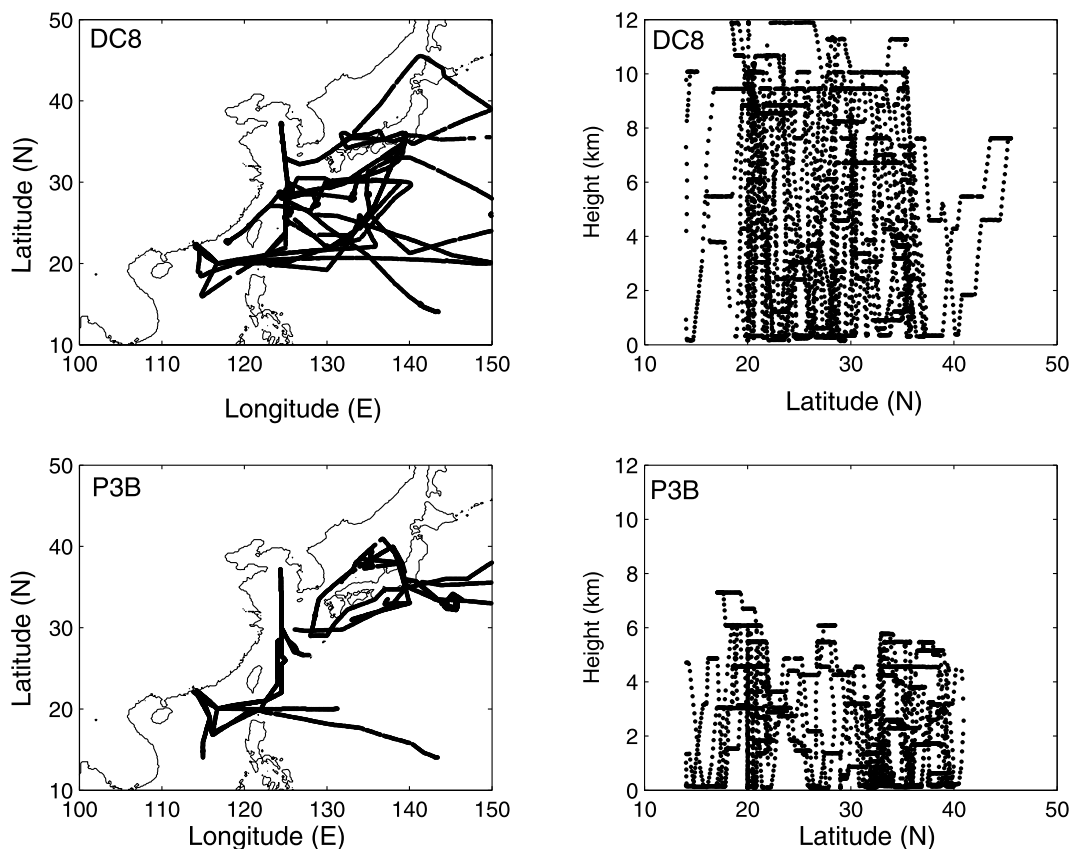


**Figure 1.** Flight tracks for the DC-8 (top panels) and the P-3B (bottom panels) during the NASA TRACE-P campaign (February–April 2001). Only 1-min flight sampling for latitudes 14N to 46N and longitudes 100E to 150E are shown and analyzed. Left panels show latitude-longitude sampling, and right panels show latitude-height sampling.

IFS meteorological fields this is shown to reproduce the stratospheric intrusions observed over the western Pacific during TRACE-P [Wild *et al.*, 2003]. The simulation of CO shows a small negative model bias [Kiley *et al.*, 2003], but the variation of CO with latitude, altitude, and time are captured reasonably well.

[8] We define an extended TRACE-P 4-D domain covering most of the measurement flights during the campaign over the east Asia-western Pacific region: Each CTM grid cell from 14N to 46N and 100E to 150E up to 18 km height from 3 March to 3 April 2001. Photochemical results from the CTM are saved hourly over this domain to make a 4-D data set. Figure 1 shows DC-8 and P-3B flight tracks in both plan view and vertical cross section. Only sampling points that fall in the extended 4-D domain (14N–46N, 100–150E) are shown. CTM simulations of flight-track observations of CO and O<sub>3</sub> are interpolated from the 4-D data to the exact location of the DC-8 and P-3B aircraft at 1-min intervals along their flight tracks. Similarly, CTM simulations of lidar data are constructed to compare with the DIAL O<sub>3</sub> lidar measurements made on the DC-8 aircraft [Browell *et al.*, 2003]. The reported 1-min O<sub>3</sub> lidar observations have data missing occasionally due to cloud obscuration or instrumental downtime. We derive simulated-lidar profiles from the 4-D CTM data that miss the same data points. We also calculate a second set of simulated O<sub>3</sub> vertical profiles

along each DC-8 flight track assuming perfect profiling from the surface to 18 km.

## 2.2. Adaptive Kernel Estimation Method

[9] Adaptive kernel estimation method has been used widely in climate research to construct PDFs and locate the maxima identifying climate regimes [Kimoto and Ghil, 1993; Corti *et al.*, 1999; Hsu and Zwiers, 2001]. The method is able to analyze unevenly and sparsely distributed data by considering a varying window width of the kernel, and thus it produces PDFs where data are sparse without spurious local maxima [Silverman, 1986]. Such an approach is needed to derive continuous 2-D PDFs from the O<sub>3</sub>–CO correlations observed in TRACE-P.

[10] The kernel-type probability density function estimator has the form

$$\hat{f}(\mathbf{x}) = \frac{1}{N} \sum_{i=1}^N H^{-n} \eta_i^{-n} K\left(\frac{\mathbf{x} - \mathbf{X}_i}{H\eta_i}\right), \quad (1)$$

where  $\mathbf{x}$  is an arbitrary point in the  $n$ -dimensional space,  $\mathbf{X}_i$  represents a data point in this space, and  $N$  is the sample size. For our specific problem, we compute the 2-D PDF over the CO–O<sub>3</sub> domain (i.e.,  $n = 2$ ).  $K(\cdot)$  assigns weights that depend upon the relative proximity of  $\mathbf{x}$  and the data points. This function is called the kernel function and is



chosen to be the Gaussian kernel, i.e.,  $K(\mathbf{x}) = \frac{1}{2\pi} \exp(-\mathbf{x}'\mathbf{x}/2)$ , with  $t$  denoting transpose. The width of the kernel function is determined by a smoothing parameter,  $H$ , weighted by the local data density  $\eta_i$ , which is inversely proportional to the square-root of the probability density at sample point  $i$ . Thus a pilot estimation of  $\hat{f}(X_i)$  is required to compute  $\eta_i$  for which  $\hat{f}(\mathbf{x})$  is calculated with a fixed window width  $h_{\text{pilot}} = 0.96N^{-1/6}$ . The optimal value of the smoothing parameter,  $H$ , is determined by minimizing the score function  $M(H)$  which is the integrated square error between the estimator  $\hat{f}(\mathbf{x})$  and the true density  $f(\mathbf{x})$ . The score function  $M(H)$ , can be approximated as:

$$M(H) \equiv \int (f - \hat{f})^2 dx \approx \int \hat{f}^2 dx - 2/N \sum_{i=1}^N \hat{f}_i(X_i) \quad (2)$$

where  $\hat{f}_i(X_i)$  is the probability density estimated at sample  $i$  with the estimator that is obtained when  $i_{th}$  sample is removed. The detailed derivation can be found in *Silverman* [1986]. A numerical routine is set up to find the minimum of the score function and extract the optimal smoothing parameter and compute the PDF as in equation (1).

[11] We apply this method to the TRACE-P in situ measurements, combining all DC-8 and P-3B flights. The same method is used for the CTM simulations of these in situ measurements. For the large and evenly distributed 4-D CTM data set, however, this method is computationally infeasible and unnecessary, and we use the conventional 2-D histogram with a Laplacian filter to smooth the edges of the distributions.

### 2.3. Empirical Orthogonal Analysis of Ozone Lidar Profiles

[12] EOF analysis has become one of the more commonly used multivariate statistical tools in atmospheric sciences since *Lorenz* [1956] introduced this method (see also *Wilks* [1995]). In climate studies, for example, recent EOF analysis [*Thompson and Wallace*, 1998, 2000] has sparked tremendous interest in detecting the climate signal of downward propagation from stratosphere to troposphere [e.g., *Baldwin and Dunkerton*, 1999], and in atmospheric chemistry it has been used to relate the spatial distribution of lightning (and the odd-nitrogen it generates) with the expected anomalies in tropospheric  $O_3$  [*Martin et al.*, 2000]. EOF analysis is particularly effective when the EOF patterns can be associated with geophysically meaningful patterns, e.g., in the climate studies above the first EOF is characterized with a more or less annular structure and is named the Arctic Oscillation or Northern Annual Mode. On the other hand, such studies can ignite disputes over whether the EOFs obtained from statistical analysis are real physical modes [e.g., *Dommenget and Latif*, 2002].

[13] In our study we use EOFs to identify the typical vertical structures of the  $O_3$  profiles as measured by the lidar and as simulated in the CTM. Assume that there are  $N$   $O_3$  profiles, spanning a range of horizontal space and time, and that each profile  $y_k$  is resolved by  $k = 1$  to  $K$  vertical levels. The  $O_3$  anomaly matrix  $Y'_{K \times N}$  is constructed from these  $N$  vectors of rank  $K$  with the mean profile  $\bar{y}_k$  subtracted (i.e., centered data). Because the vertical levels are uneven, we choose to weight each row of  $Y'$  by the square root of that level thickness ( $dZ_k^{1/2}$ ).  $S_{K \times K}$  is

basically the product of the anomaly matrix  $Y'$  and its transpose  $Y'^T$ .

$$S = \frac{1}{N-1} Y' Y'^T. \quad (3)$$

Points in an  $O_3$  profile where data are missing are skipped and do not contribute to the covariance matrix. The degrees of freedom are no longer  $N-1$  as in the denominator in equation (3), but this factor is taken inside the matrix and varies with each element of  $S$  depending on the number of nonzero elements in the cross-multiplication between different vertical levels of  $O_3$  anomalies.

[14] The eigenvectors  $\hat{e}_i$  of the covariance matrix are the  $K$  solutions to equation,  $S\hat{e}_i = \lambda_i \hat{e}_i$ , where  $\lambda_i$  are the eigenvalues. The eigenvectors are of rank  $K$ , and each element corresponds to a vertical level. The EOF vectors  $e_i$  are then the eigenvectors rescaled at each level by the inverse of the weights used in calculating the anomaly matrix, i.e., dividing each element of the vector  $\hat{e}_i$  by the square root of the level thickness. We use normalized EOFs such that the inner product of each EOF vector using the level thickness as the weighting is unity,  $\sum_{k=1}^K e_i^k e_i^k dZ_k = 1$ . The proportion of the total variance represented by the  $i^{th}$  EOF vector is  $\lambda_i / \sum_{i=1}^K \lambda_i$ .

[15] Any  $O_3$  profile  $y$  can be expressed in terms of the mean profile  $\bar{y}$ , the EOFs, and their Principal Components  $a_i$  (PCs),

$$y = \bar{y} + y' = \bar{y} + \sum_{i=1}^K e_i a_i. \quad (4)$$

Because of orthogonality of the EOFs, the PCs are readily calculated by projecting the centered data onto the normalized EOFs and have units of ppb (parts per billion as mole fraction) of  $O_3$ ,

$$a_i = e_i^T \cdot y'. \quad (5)$$

The number of EOFs can be very large and depends on the vertical resolution in this case, but as with most studies, we focus only on those EOFs with the largest eigenvalues since they describe most of the variance. What is different in this study, however, is that each  $O_3$  profile is collected over a range of horizontal space and time. Hence the PCs are not just time series as in most published analyses but vary with geographic location as well.

[16] The extended 4-D CTM data set for the TRACE-P domain gives  $N = 373248$   $O_3$  profiles. For the observed lidar data,  $N = 4871$  profiles. For the CTM data interpolated onto DC-8 Flight tracks to match the 1-min lidar profiles, two data sets are used: Exact lidar simulations with missing data and complete profiles along the flight tracks. To prevent the overwhelmingly large variance of stratospheric ozone from dominating the analysis, we confine analysis to heights below 8.3 km. For CTM data this corresponds to  $K = 24$  vertical levels, and for the lidar observations this is interpolated onto 140 levels.

### 3. Cumulative Probability Distributions of CO and $O_3$

[17] The cumulative probability distributions of the observed CO and  $O_3$  abundances show a population that



**Table 1.** Number of Data Points (N) for CO and O<sub>3</sub> From DC-8 and P-3B In Situ Flight Measurements, O<sub>3</sub> Lidar Data Along DC-8 Flight Tracks, and CTM Data for the Extended 4-D Domain<sup>a</sup>

	0–1 km	1–10 km	10+ km
<i>Sample size (N) for CO in situ data</i>			
14–25N	793	3135	434
25–46N	1624	4337	241
<i>N for O<sub>3</sub> in situ data</i>			
14–25N	821	3305	486
25–46N	1736	4638	271
<i>N for O<sub>3</sub> lidar data</i>			
14–25N	35814	0.29 M	0.13 M
25–46N	33300	0.27 M	75431
<i>N for extended 4-D domain</i>			
14–25N	1.0 M	2.8 M	0.3 M
25–46N	1.4 M	5.2 M	0.5 M

<sup>a</sup>The sample size of the extended 4-D data for 10+ km listed below is from 10–12 km. To compare with the lidar data, the 4-D domain is extended to 18 km and the sample size is 4 times larger than the numbers shown above.

can be separated into background levels (typically the central 50% or more of the population) and into pollution events or stratospheric intrusions (evident in the extreme abundance ranges). Our CTM simulated probability distributions of this flight-track data are a direct test of our ability to represent these populations for the TRACE-P sampling of the domain. Moreover, the same probability distributions from the extended 4-D domain can identify whether the TRACE-P sampling is representative of the larger domain.

[18] We recognize that different parts of the domain will have different extreme populations and background levels, and thus we have split the domain into tropical (14N–25N) and extratropical (25N–46N) as well as boundary layer (0–1 km), free troposphere (1–10 km), and region of stratospheric influence (10–12 km) where air of stratospheric origin are more likely to be sampled. The boundaries are somewhat arbitrary but we found that these choices sufficiently highlighted the different probability distributions in the observations. Table 1 gives the number of data points, N, for CO and O<sub>3</sub> in situ measurements along the combined DC-8 and P-3B flight tracks, O<sub>3</sub> measurements from DC-8 lidar sampling, and the sampling from CTM in the extended 4-D domain. N increases by about 2 orders of magnitude from in situ measurement to lidar sampling, and by about 1 order of magnitude from lidar sampling to 4-D model data sampling. Table 2 summarizes the 25th percentile (first quartile or Q) and the 50th percentile (median or M) for the observations, the simulated observations along flight tracks, and the simulated distributions of the extended 4-D domain. The cumulative probability distributions for CO are plotted in Figure 2a as a function of sigma,  $\sigma$ , the standard deviation of the normal distribution. Vertical dashed lines mark the 25% (Q,  $\sigma = -0.675$ ) and 50% (M,  $\sigma = 0$ ) probabilities. In each of the six regions, the observed distribution (solid line) is compared with the simulated observations (dashed line). The overlap of these distributions is a measure of the accuracy of the CTM in simulating the TRACE-P observations.

[19] Below the 50th percentile, the CO distribution is extremely well simulated (typically within 5 ppb) by the

model for all regions except the tropical boundary layer where the CTM uniformly underestimates the observed CO by about 12 ppb. In CTM sensitivity tests with a range of CO-like tracers (not shown here), we find that much of the observed variance (e.g., as measured by M - Q), including fine-scale features, is driven by large and synoptic-scale systems acting on the global-scale latitudinal gradients in CO, rather than by the nearby east Asian emissions. Thus we take this agreement to mean that the large-scale CO gradients and meteorological systems are well simulated. Above the 75th percentile, however, the simulations are uniformly much smaller than observed. One cause might be the failure of the CTM to resolve urban plumes, for example, the intense, small-scale pollution events such as the Shanghai plume [Russo *et al.*, 2003; Simpson *et al.*, 2003; Talbot *et al.*, 2003]. However, for the distributions shown in the figure (CO < 300 ppb), the observed probability distributions are unaffected by spatial filtering at the CTM resolution, and hence these probability distributions should be resolved by the model. Thus the uniform underprediction of the CO probabilities at the upper end of the distribution as shown are likely due to an underestimate of CO emissions from east Asian sources [Palmer *et al.*, 2003] or possibly to chemical influences rather than lack of model

**Table 2.** TRACE-P In Situ CO and O<sub>3</sub> Percentile Levels (in ppb) Compared With the CTM Simulation Along the Flight Tracks and for the Extended Domain<sup>a</sup>

	0–1 km	1–10 km	10+ km
<i>Q:M for in situ CO OBS</i>			
14–25N	140:185	86:108	80:87
25–46N	205:226	114:138	68:89
<i>Simulated OBS</i>			
14–25N	130:171	90:99	81:94
25–46N	201:214	119:139	66:101
<i>Extended domain</i>			
14–25N	116:149	88:100	85:95
25–46N	178:207	113:137	15:45
<i>Q:M for in situ O<sub>3</sub> OBS</i>			
14–25N	28:46	33:48	22:29
25–46N	53:57	53:58	65:69
<i>Simulated OBS</i>			
14–25N	31:49	29:34	26:29
25–46N	66:70	51:59	50:94
<i>Extended domain</i>			
14–25N	22:39	26:36	24:33
25–46N	58:62	53:60	85:225
<i>Q:M for Lidar O<sub>3</sub> OBS</i>			
14–25N	28:41	32:46	24:36
25–46N	47:54	53:58	50:69
<i>Simulated Lidar OBS</i>			
14–25N	32:48	29:35	25:33
25–46N	62:69	51:59	45:75
<i>Extended domain</i>			
14–25N	22:39	26:36	24:37
25–46N	58:62	53:60	158:500

<sup>a</sup>The 25th percentile (1st quartile or Q) and the 50th percentile (Median or M) values are given as pairs (Q:M). For O<sub>3</sub> the lidar observations and CTM simulations are also shown. See the text and Figures 2 for details.

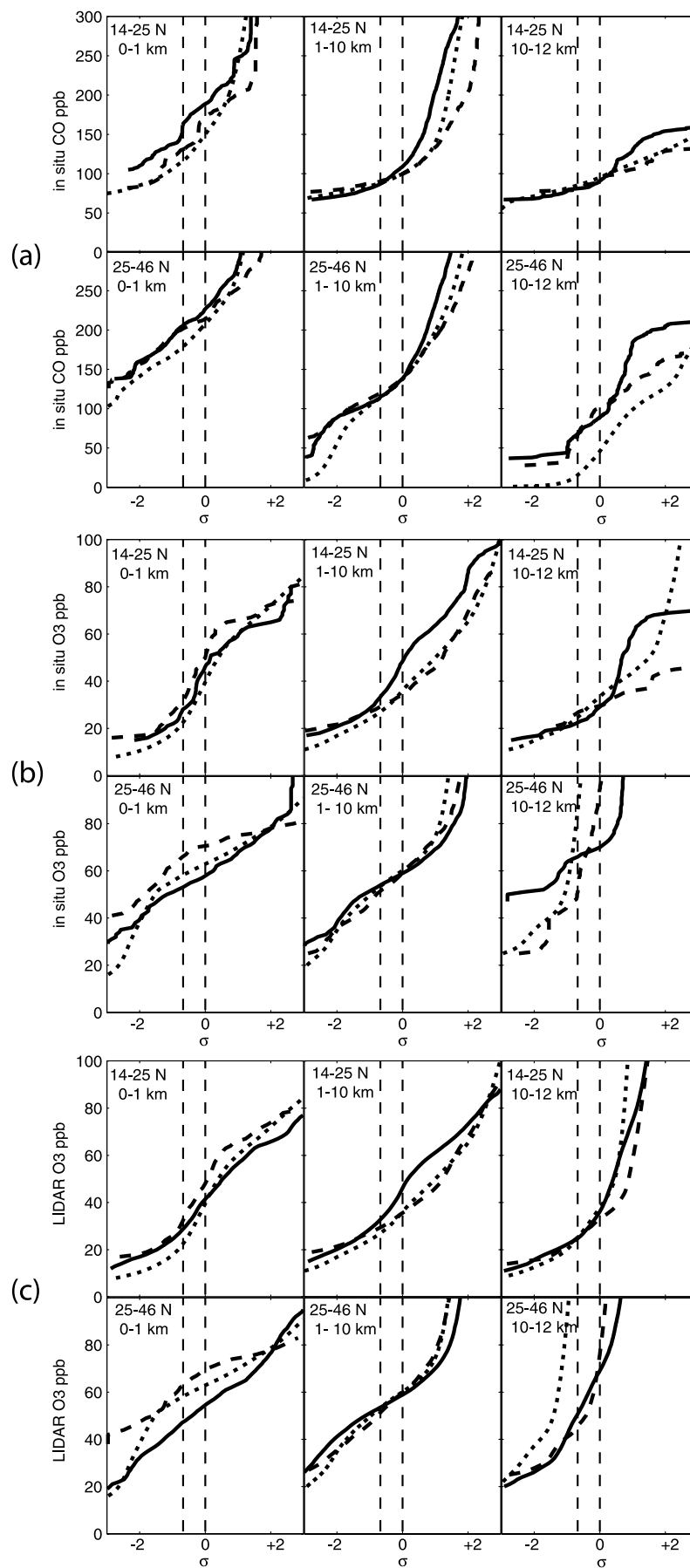


Figure 2.

resolution (more supporting evidence from the  $\text{O}_3$ -CO correlations is presented in section 4).

[20] The difference between the flight-track simulations (dashed line) and the extended-domain probabilities (dotted line) is also shown in Figure 2. These latter distributions have three orders of magnitude more points than the in situ sampling and hence smoother curves. In the free troposphere the Q and M values show no obvious statistical bias, but in the boundary-layer there is a preference for sampling higher CO, a possible indication of chasing pollution outflow from the continent. For CO abundances greater than 200 ppb at all heights, the extended-domain sampling includes values over the continent and thus shows greater probabilities for these high-CO events than the simulated flight tracks. The extremely low CO abundances in the extratropics (1–10 km and 10–12 km) indicate air of stratospheric origin, and their frequency ranges from a few percent below 10 km height to as much as 50% in the 10–12 km region. The flight track sampling greatly underestimates their frequency both above and below 10 km height; this reflects the strong latitude and height gradients over this domain and sampling that is preferentially toward the southern and the lower part of the range.

[21] Ozone comparisons show both successful simulations and some obvious model errors. In the free troposphere the observed extratropics probability distribution for the in situ data (Figure 2b) is well matched by the model for the central 50% of the distribution. In the tropics, however, the model accurately matches only the lowest 25% of the distribution and consistently underestimates ozone in the remaining 75 percent of the distribution by 10 ppb or more. For the boundary layer, the model is biased high for both tropics and extratropics. The offset between boundary layer and free troposphere is large and consistently in error for all latitudes: Observations have a shift of about +5 ppb (boundary layer being less than free troposphere for both Q and M); the model predicts an opposite shift of about –10 ppb. This model error can best be explained if the continental boundary-layer sources of ozone from Asia are exaggerated [Wild *et al.*, 2003]. A separate error, the underestimate of tropical ozone (and also the upper 50% of CO) could be due to a missing source, most likely from an underestimate of the episodic emissions from biomass burning and lightning during the TRACE-P period.

[22] For stratospherically influenced regions the comparison with in situ data is erratic due to the small number of points and the large variability induced mostly by stratospheric intrusions. If we expand the comparison to

the DC-8 lidar data (Figure 2c), the number of these high-altitude points increases from a few hundred to a hundred thousand and the probability distributions become well defined. For this sampling the model successfully matches the observations for the lowest 50% of the distribution and predicts about the right frequency of the stratospheric influence ( $\text{O}_3 > 100$  ppb). Including the lidar data does not change the previous conclusions and only reemphasizes the systematic error in the boundary layer found with the in situ data (see also later discussion on ozone EOFs).

#### 4. Latitude-Height Distributions of $\text{O}_3$ From the Lidar Sampling

[23] The latitude-height distribution of tropospheric  $\text{O}_3$  can help identify the tropopause, stratospheric intrusions, pollution events, and the large-scale gradient between tropics and extratropics. The  $\text{O}_3$  lidar data from TRACE-P provide the extensive sampling needed to define this latitude-height section [Browell *et al.*, 2003]. Here, we examine the probability distributions of these latitude-height sections, showing how the sequence from 10th, to 50th, to 90th percentiles (Figure 3) can be used to identify the statistical distribution of tropopause heights, those regions impacted by stratospheric intrusions, and the representativeness of the TRACE-P sampling. Each percentile figure shows the observations (top panel), the CTM simulation along flight tracks (middle panel) and the CTM simulation of the extended 4-D domain (bottom panel). The CTM simulation along the flight tracks follows the lidar sampling with data points missing; while the extended domain statistics assume that  $\text{O}_3$  is measured from 0 to 18 km, even in the presence of clouds. The white reference line in the extended-domain plots marks the upper boundary of the flight-track data used in the analysis.

[24] In the tropics, there is clear evidence of a high-ozone region at 5–10 km height near 17°N in the TRACE-P sampling. It is seen in both the observations and the CTM. This region is clearly seen at all percentiles from 10th to 90th, and moreover the ozone abundance increases slowly from about 45 ppb at the 10th percentile to about 75 ppb at the 90th percentile indicating an extensive region of low variability. Even at the 90th percentile, the ozone abundance remains well below stratospheric intrusion levels. This region was sampled on DC-8 Flight 6, and the high  $\text{O}_3$  levels have been attributed to biomass burning [Browell *et al.*, 2003]. The TRACE-P sampling clearly singles out this event (i.e., it is not seen on the extended domain) and shows

**Figure 2.** (a) CO cumulative probability distributions (in ppb of CO) as a function of standard deviation of the normal distribution ( $\sigma$ ). The 25 percentile ( $\sigma = -0.675$ ) and 50 percentile (median,  $\sigma = 0$ ) are shown as vertical dashed lines. The distribution from the combined DC-8 and P3-B in situ observations (solid line) is compared with that from the CTM simulation of these in situ measurements (dashed line). Also shown is the cumulative probability distribution from the 4-D CTM data for the extended TRACE-P domain below 12 km height (dotted line). The data set has been broken into six panels by latitude (tropical = 14°N–25°N (top) versus extratropical = 25°N–46°N (bottom)) and height range (0–1 km (left) versus 1–10 km (center) versus 10–12 km (right)). See Table 1 for the number of data points defining each distribution and Table 2 for the 1st Quartile and Median values. (b) Same as Figure 2a, but for  $\text{O}_3$  cumulative probability distributions (in ppb of  $\text{O}_3$ ) based on in situ sampling along flight tracks. (c) Same as Figure 2b, but for  $\text{O}_3$  lidar observations and simulations along DC-8 flight tracks. The CTM simulated lidar profiles have the same missing data as the lidar observations. The 4-D data extend to 18 km height.



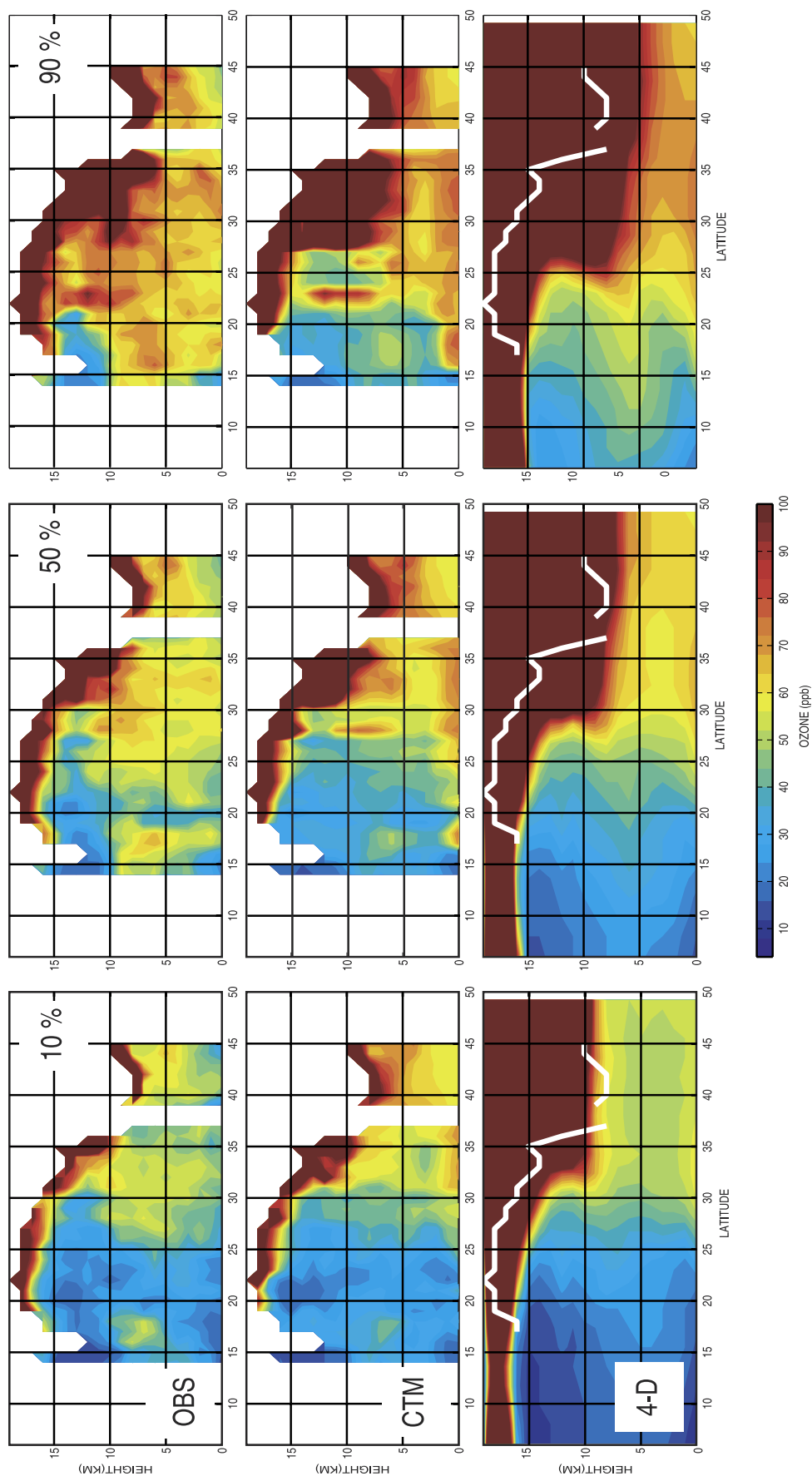


**Figure 3.** The (a) 10th, (b) 50th, and (c) 90th percentile of the O<sub>3</sub> latitude-height distribution (ppb) in the extended domain. The data are binned by 1° latitude by 1 km height bins centered at integer latitude and height. (Top row) the TRACE-P lidar observations are compared with (middle row) the CTM simulations of the lidar and with (bottom row) the extended 4-D CTM data set (100E–150E, 3 March to 3 April 2001).

the success of the CTM simulation in reproducing it at all statistical levels. Overall in the free troposphere, the CTM underestimates ozone abundance by about 10 ppb as seen also in the probability distributions in Figures 2b and 2c.

[25] In the midlatitudes, the region of high ozone abundance at 6–12 km near 28°N can be clearly seen as the remnant of a stratospheric intrusion; at the 10th percentile it has similar enhancements to the 17°N region, but the ozone abundance jumps to more than 75 ppb at the 50th percentile and become merged into the stratosphere (>100 ppb) at the 90th percentile. Several flights intercepted stratospheric intrusions in this region behind midlatitude cyclones, indicated in situ measurements by low CO and high wet-bulb potential temperatures (Mari et al., submitted manuscript, 2004). However, the greatest contributions to the O<sub>3</sub> feature at 28°N come from DC-8 Flight 16, which made a transect at this latitude on 30 March and intercepted a deep intrusion. The greater sampling along this transect explains why the feature is clearly seen in the median as well as the high end of the distribution. Another stratospheric intrusion, visible only at the 90th percentile, is observed in the tropics at 22°N between 7–14 km; while several flights contributed to the statistics over this region, a stratospheric intrusion was sampled on only one flight (DC-8 Flight 14). The CTM simulation captures this intrusion, but it occurs at a slightly lower altitude and a little further north. In summary, the CTM captures the basic statistical features of these intrusions along the flight tracks. It simulates the distribution of elevated-ozone (55–95 ppb) as it mixes into the troposphere through the range of percentiles. This success, plus the overall excellent simulation of TRACE-P ozone, ozone sondes, TOMS ozone columns, and the global mean stratosphere-to-troposphere ozone flux [Wild et al., 2003] indicates a good simulation of the dispersion and mixing of stratospheric intrusions.

[26] The statistics for the extended domain show a layer of enhanced ozone, apparently of stratospheric origin, extending from the subtropical break in the tropopause down into the tropics at about 6 km height. At all percentiles, however, they show none of the individual features picked up by the TRACE-P flight tracks. Thus tropical ozone appears to be enhanced in the midtroposphere by stratospheric ozone mixing down from the subtropical jet. In comparing the CTM flight tracks with the extended domain, it is clear that the TRACE-P mission favored sampling of pollution sources with enhanced boundary-layer ozone, but this only emphasizes the CTM exaggeration of boundary-layer ozone when compared with observations, as discussed above. All three latitude-height sections show the descent of stratospheric air (as measured by the 100 ppb contour) by 2–3 km in height as one progresses from 10th to 90th percentile.

## 5. Probability Density Function in CO-O<sub>3</sub> Domain

[27] The patterns of correlation between CO and O<sub>3</sub> can identify mixing between different chemical regimes in the atmosphere and further provide information on the photochemical evolution of O<sub>3</sub> in polluted plumes [Parrish et al., 1993]. A first approach to O<sub>3</sub>-CO correlations is to examine the scatter plots for all in situ measurements. As an example, the one-minute in situ measurements from DC-8 flights 13 and 15 are compared with the CTM

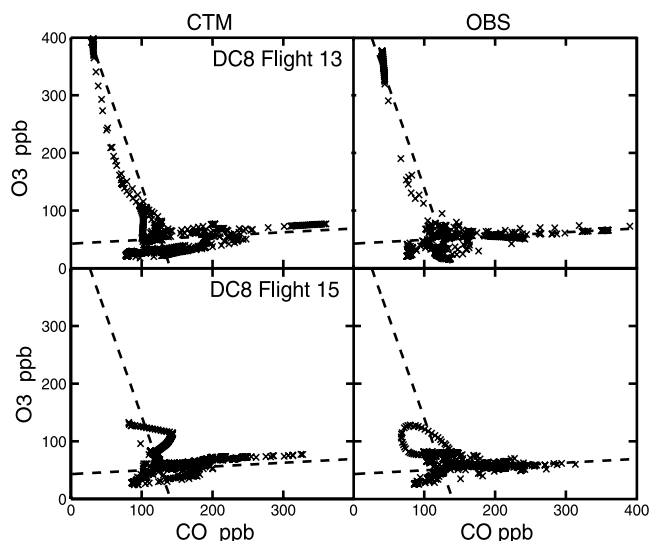


**Figure 4.** O<sub>3</sub>-CO scatter plots (ppb versus ppb) for DC-8 flights 13 and 15. TRACE-P observations are compared with FRSGC/UCI CTM simulations.

simulation in Figure 4. In this analysis, the 1-min observations are taken as is, with no spatial smoothing to match the CTM grid. In the figure, the dashed lines (the same in all panels of Figures 4 and 5) are a least-squares fit to all observations for low-CO and high-CO regions (see Figure 5 caption or text below). DC-8 flights 13 and 15 show occurrences of low-CO stratospheric air that are well simulated, including both magnitude and slope.

[28] Model simulations of individual flights are generally excellent, agreeing with the observation of stratospheric air (low CO, very high O<sub>3</sub>) and pollution plumes (high CO, moderate O<sub>3</sub>). A combined scatter plot with all the data points would not be easy to interpret, and thus we apply adaptive kernel estimation (section 2.2) to derive two-dimensional probability density functions (PDF) for both measurements and model. The adaptive kernel method generates smooth PDFs without spurious maxima from the more than 10,000 individual points as shown in Figure 5.

[29] In calculating these PDFs, we have chosen to spatially smooth the observations to more closely match the CTM grid. The observations show distinct features on very small scales, such as 100-m thick laminae, which cannot be resolved by the CTM grid (about 500 m vertical by 180 km horizontal). Thus we define a triangular weighting function with a half-height, half-width of 500 m in the vertical and 180 km in the horizontal, and we process the 1-min in situ observations from each flight according to their vertical and horizontal separations. For each point all measurements that fall within a 180 km radius and within 500 m in height contribute to the value at that point.

[30] The top panel in Figure 5 shows the PDF for the observed CO-O<sub>3</sub> data points during TRACE-P. The contours are logarithmic (base 10) and denote the probability per unit area in ppb<sup>2</sup>. For example, the probability of observing CO between 200 and 201 ppb at the same time as O<sub>3</sub> between 50 and 51 ppb is about 10<sup>-4</sup>. The integral of the PDF over the entire range up to 1000 ppb in CO and O<sub>3</sub> is nearly 1. The middle panel of Figure 5 shows the

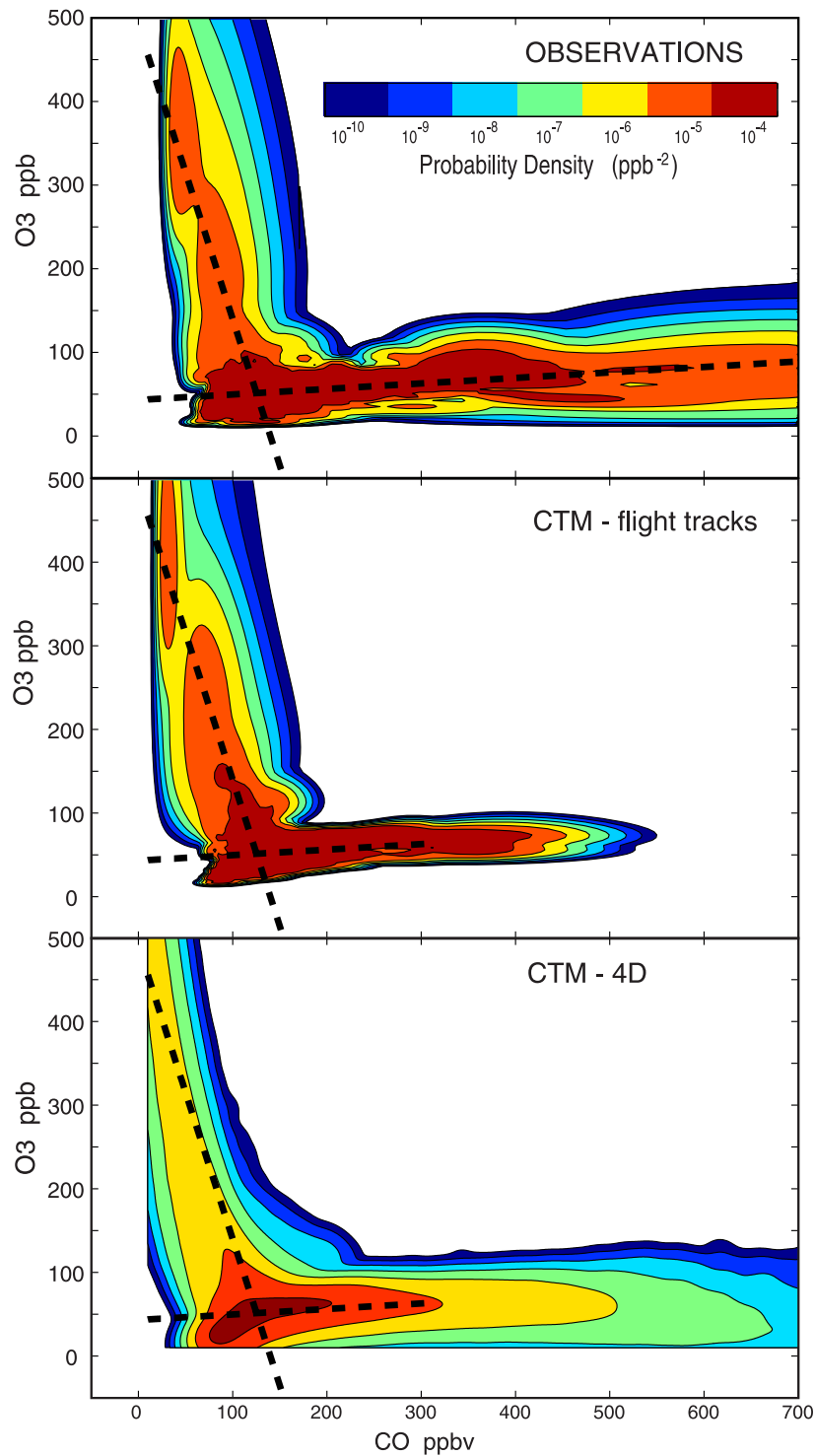


**Figure 5.** Probability density (per unit ppb<sup>2</sup> area) in the CO-O<sub>3</sub> domain plotted in a log base-10 scale. The probability density over the entire CO-O<sub>3</sub> domain up to 1000 ppb (not plotted) integrates to 1. Top panel shows the in situ measurements from the combined DC-8 and P-3B flights, middle panel shows the CTM simulation of those in situ data, and the bottom panel shows the extended CTM 4-D data set from the TRACE-P domain sampled below 12 km height. The thick dashed lines, the same in all three panels, are simple linear regression lines from the observed data: The left line for O<sub>3</sub> > 100 ppb and CO < 200 ppbv, and the right line from the remainder of the data.



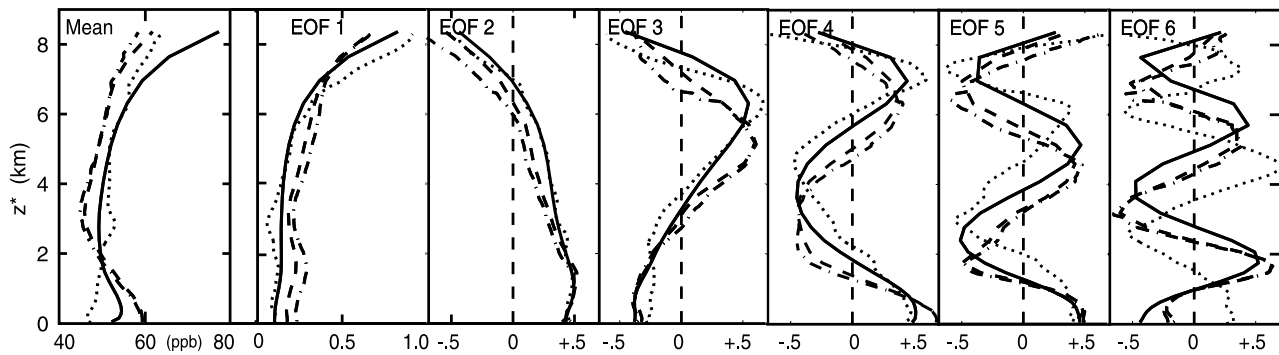


**Figure 6.** The  $\text{O}_3$  profiles mean value (ppb) and first 6 normalized EOFs (dimensionless) up to 8.3 km height. Different sets of  $\text{O}_3$  data include the extended CTM 4-D domain (solid), the complete CTM profiles along DC-8 flight tracks (dashed), the observed lidar profiles (dotted), and the CTM simulation of the lidar which miss the same data points as the observations (dash-dot). See text.

equivalent PDF for the CTM flight-track data; and the bottom panel, for the extended 4-D domain. The dashed line in all three panels is the same: The small positive  $\text{O}_3/\text{CO}$  slope (+0.06) is a fit to the spatially filtered observations that generally describe background plus pollution events ( $\text{CO} > 200$  ppb or  $\text{O}_3 < 100$  ppb); the large negative slope ( $-3.4$ ) is a fit to the stratospherically influenced air ( $\text{CO} < 200$  ppb and  $\text{O}_3 > 100$  ppb).

[31] Both observed and modeled flight-track PDFs show almost identical patterns of stratospheric influence, even to the bimodality due to TRACE-P sampling that is not seen in the extended-domain PDF. The probability of high- $\text{O}_3$  intrusions is accurately modeled in terms of magnitude, slope, and probability. The high- $\text{CO}$  region, unfortunately, is not well simulated. Even with the spatial filtering, the observations show a significant probability for  $\text{CO} > 500$  ppb, where the CTM shows none. On the other hand, the high- $\text{CO}$  regions of greater probability (i.e., orange:  $\text{PDF} \geq 10^{-5}$  per  $\text{ppb}^2$ ) are well modeled. There is a clear statistical bias in which the CTM TRACE-P flight tracks have this probability region extending to 400 ppb (both observations and model), whereas the extended CTM 4-D domain has it extending only to 300 ppb.

[32] The  $\text{O}_3/\text{CO}$  slope for the high- $\text{CO}$  events is often used to infer the amount of  $\text{O}_3$  exported from regional pollution [Parrish *et al.*, 1993]. Taking the TRACE-P statistics as a whole, rather than selecting individual events, we find that the derivation of a single slope to characterize the observations is difficult. The mean slope of +0.06 accurately characterizes the very high probability region (red,  $\text{PDF} \sim 10^{-4}$  per  $\text{ppb}^2$ ), but this slope is smaller for the moderate-to-lower probability regions that characterize  $\text{CO} > 300$  ppb. For both model and measurements, the  $\text{O}_3/\text{CO}$  slope for this extended region is almost zero. In varying different criteria for selecting the data (e.g., considering only  $\text{CO} > 200$  ppb, tropics versus extratropics), we find that this  $\text{O}_3/\text{CO}$  slope varies considerably and includes also small negative slopes. This is consistent with measurements made at Sable Island in pollutant outflow from North America, where the correlation of  $\text{O}_3$  and  $\text{CO}$  is very poor in spring and autumn, and the ratio is close to zero in March [Parrish *et al.*, 1993]. One consistent picture from

the observations is that the slope in the tropics (e.g., 0.08 for  $\text{CO} > 200$  ppb) is greater than that in the extratropics (0.03 for  $\text{CO} > 200$  ppb). Both values are much less than that derived from a simple mixing curve between the median values of  $\text{O}_3$  and  $\text{CO}$  in the tropics and extratropics (about +0.3). Use of the  $\text{O}_3/\text{CO}$  slope alone as a test of photochemistry or a measure of  $\text{O}_3$  production will require analysis on a case-by-case basis, and it is likely to work less well in spring than during summer when  $\text{O}_3$  production is more rapid.

## 6. Empirical Orthogonal Function Analysis of Ozone Profiles

[33] The dense vertical sampling of  $\text{O}_3$  by lidar allows us to characterize the vertical structures of ozone over the west Pacific. We analyze the covariance matrix constructed from the horizontal-temporal sampling of  $\text{O}_3$  vertical profiles up to a height of 8.3 km, as described in section 2.3. The EOFs (dimensionless) are patterns of vertical structure of the variance about the mean profile. The Principal Components (PCs, in units of ppb) are the coefficients of the EOFs (one for each EOF) derived from fitting a single profile to the mean profile plus EOFs. In this study each profile, and hence each set of PCs, is a function of latitude, longitude, and time.

[34] The six leading, normalized EOFs plus the mean profile are shown in Figure 6 for the lidar observations and for three different ways of sampling the model. The EOF vertical structures, even to EOF-6, are remarkably similar across all four data sets. There is a tendency for the lidar-observation EOFs (dotted lines) to look more like those from the extended 4-D domain (solid lines) rather than flight-track EOFs (dot-dashed and dashed lines). Within the CTM data there is a systematic downward shift in the EOF structures for the TRACE-P flight tracks relative to the extended 4-D domain but hardly any difference due to the lidar missing data (dashed versus dot-dashed). The impact of missing data is also barely visible for the mean profile. The mean profile from either of the CTM data sets re-emphasizes the model error in boundary-layer  $\text{O}_3$  with a vertical gradient opposite to observations as discussed in

**Table 3.** Variance in Percentage (%) Captured by the First Six EOFs

EOFs	1	2	3	4	5	6
Lidar Observations	57.41	20.38	8.89	4.29	2.31	1.42
CTM Simulated lidar	75.14	13.79	4.94	3.04	1.30	0.72
CTM Complete profiles	76.70	13.34	3.91	2.81	1.31	0.70
CTM 4-D Extended domain	80.88	11.69	3.26	1.81	0.90	0.52

section 3. The variability structures are quite reasonable up to EOF-5 or EOF-6, and hence this error is likely due to a systematic, time-independent model bias that is apparently related to the over-production of  $O_3$  in the boundary layer [Wild *et al.*, 2003].

[35] The variances (in percentage) captured by each EOF for each data set are listed in Table 3. The first six EOFs comprise 95% of the total variance from the lidar observations and 99% of that from the CTM data. This difference might be attributed to the limited vertical resolution of the model. There is a systematic difference between the model and observations in the partitioning of variance among the EOFs: The model overestimates the EOF-1 variance by a factor of 1.3 and underestimates that from EOFs 2–6 by factors between 1.4 and 2. EOF-1 appears to represent the variance due to tropopause height, and thus the overestimation of EOF-1 variance in the model is consistent with the  $O_3$  90th percentile distribution shown in Figure 3, which shows that the model predicts a lower tropopause and extensive stratospheric descent northward of 27°N.

[36] To demonstrate how these EOFs describe the  $O_3$  abundance, we reconstruct an  $O_3$  latitudinal transect at 125.6°E on 05Z 21 March by adding successive EOFs to the mean profile (shown as the leftmost panel in Figure 6) in Figure 7. At that time, DC-8 flight 13 was flying toward the Yellow Sea from 25°N to 32°N approximately along the same longitude, and the detailed meteorological analysis can be found in the work of Mari *et al.* (submitted manuscript, 2004). The top panel of the figure shows the  $O_3$  latitude-height distribution constructed from the mean profile plus EOF-1, and successive panels show the cumulative addition of EOF-2 through -6. The input  $O_3$  latitude-height distribution (panel below EOF-6) is accurately reconstructed by these six EOFs. The residual  $O_3$  (input minus reconstructed, lowest panel) shows that only small-scale, small-amplitude features remain. Some understanding of what the EOFs may represent can be seen in this sequence: EOF-1 restores the large-scale latitudinal gradient, distinguishing tropics from extratropics, especially in terms of tropopause height and large-scale descent of stratospheric air; EOF-2 restores the high  $O_3$  abundances in the extra-tropical boundary-layer and the low  $O_3$  abundances in the tropical boundary layer; EOF-3 captures the high  $O_3$  band around 5–7 km both in midlatitudes and tropics; EOF-4 reemphasizes the boundary-layer gradients; and the stratospheric intrusion (about 6 km, 25°N–30°N) is finally outlined with EOF-5 and EOF-6.

[37] The time-averaged PC distribution gives a good indication of preferred geographical locations for a given EOF. Figure 8 shows the geographic distribution of the PCs of EOF-1 through EOF-5 for the CTM extended 4-D domain (left panels, top to bottom respectively), the CTM lidar simulations (center panels), and the lidar observations (right panels).

For all three data sets (left, center, right), we project the centered data (i.e., mean profile removed) onto one set of EOFs, those derived from the 4-D CTM data (solid curves in Figure 6). For the center and right panels, thus the principal components should be denoted pseudo-PCs. Also for the center and right panels, projecting an incomplete  $O_3$  profile (even with mean removed) onto any EOFs produces large, unrealistic values; and we choose to fill the missing data with the corresponding CTM data values. Thus the observed lidar data set has all missing data replaced by modeled values and the simulated lidar data set used for the PCs have complete profiles along flight tracks. All PCs are averaged over time (3 March to 3 April 2001). For the 4-D data the horizontal resolution is that of the CTM, and for flight track data (center and right panels), the one-minute data are averaged over  $2^\circ \times 2^\circ$  bins in longitude and latitude. Note that the units are ppb of  $O_3$  and have different amplitudes for each EOF but the same scale across the three data sets.

[38] As shown in the left panels in Figure 8, PC1-PC3 have more uniform zonal distributions while PC4 and PC5 show high values just off the Asian coast in the subtropics. This pattern is consistent with the decomposition of the single transect in Figure 7: The first three EOFs capture mostly the variance associated with the large-scale  $O_3$  background, and the higher EOFs explain fine structures that tend to have more localized distributions. PC1 is mostly associated with the stratospheric influence below 8.3 km and exhibits a maximum around 135°E and 45°N, decreasing monotonically toward the tropics. PC2, whose EOF has a deep boundary-layer structure, has a maximum band around 32°N and decreasing both northward and southward, with an equally large negative minimum in the tropics. PC3, whose EOF has a maximum around 5–6 km, has a positive maximum amplitude in the tropics near 14°N and a smaller negative minimum near 22°N in the subtropics. The fact that the maximum occurs near the tropics seems to suggest that this feature is related to biomass burning. PC4 has a positive maximum distribution along the southeast coast of Asia; PC5 has a maximum located west of Taiwan and North of Hong Kong. These features, in contrast to PC1-PC3, are probably associated with variability from local pollution plumes.

[39] The CTM flight track data (center panel) capture more or less similar PC distributions to the extended 4-D results. Nevertheless, the values are higher than those from the 4-D data indicating a statistical bias, for example, in stratospheric intrusions north of Japan (PC1) and in pollution plumes near the coast (PC4 and PC5). Comparing the observed PCs (right panel) with those from the CTM flight tracks, the agreement is excellent for PC1 and PC2, quite good still for PC3 and PC4 (at least in terms of general pattern), but loses much of the coherence by PC5.

[40] In summary, this EOF/PC analysis of the TRACE-P  $O_3$  profiles has clearly quantified the statistical biases in TRACE-P sampling and identified them with specific profile structures and specific locations. In addition there is generally good agreement between model and observations for the geographic patterns of PC1 through PC4, however, some caution on this approach as a model-measurement validation tool is needed. The filling of lidar missing data with model data may have enhanced this

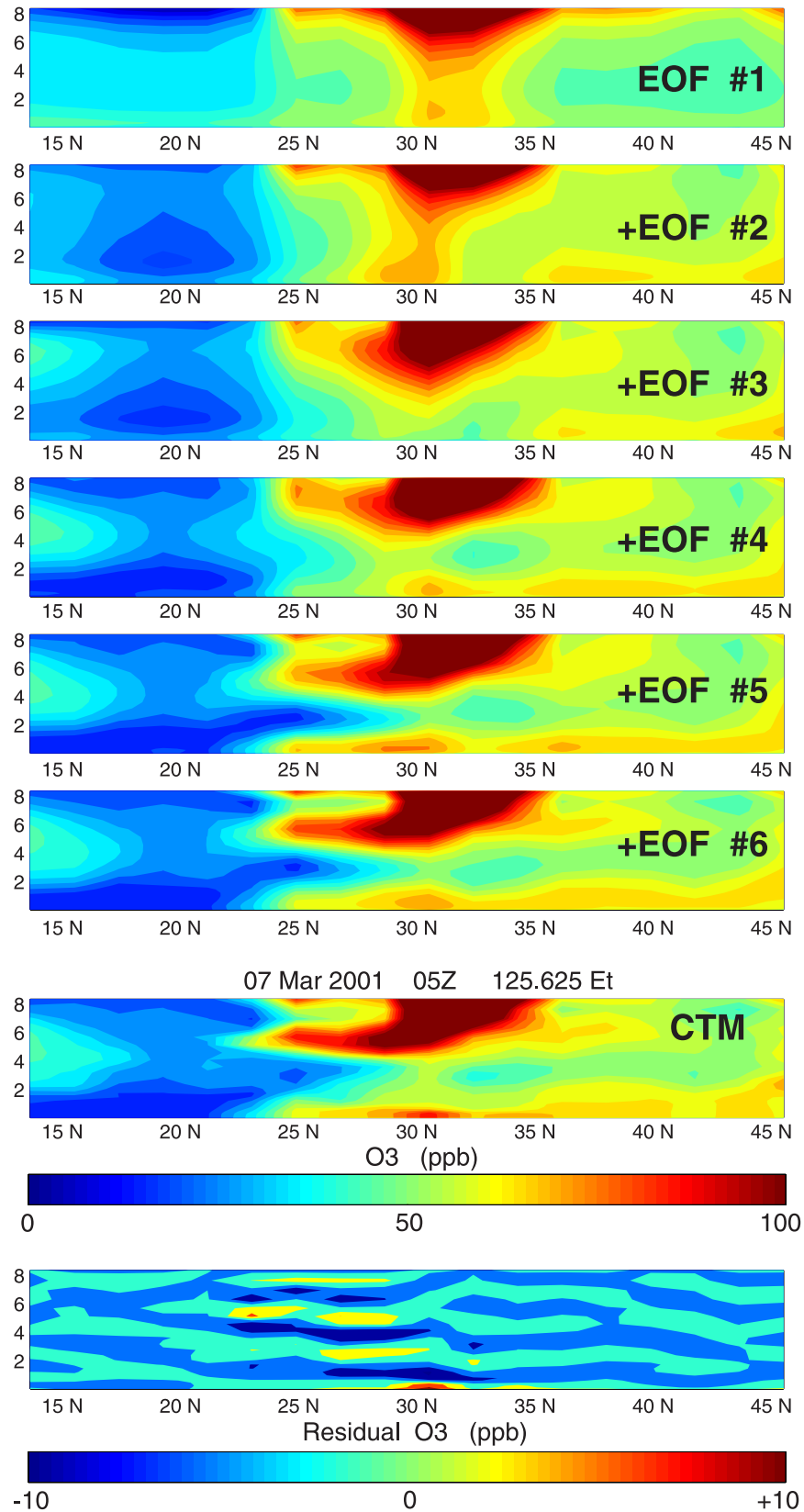


**Figure 7.** O<sub>3</sub> latitude-height transect (in ppb) from the CTM 4-D simulation at 126E at 0500Z, 21 March 2001. The top six panels show the reconstruction of this transect from the latitude-independent mean profile (solid line, first panel in Figure 6) with the cumulative addition of EOF-1 through EOF-6 (latitude independent) multiplied respectively by the values of PC1 through PC6 (latitude dependent). The CTM transect is shown in the next panel below with the same color scale. The residual (transect minus reconstruction) is shown in the bottom panel with an expanded color scale.



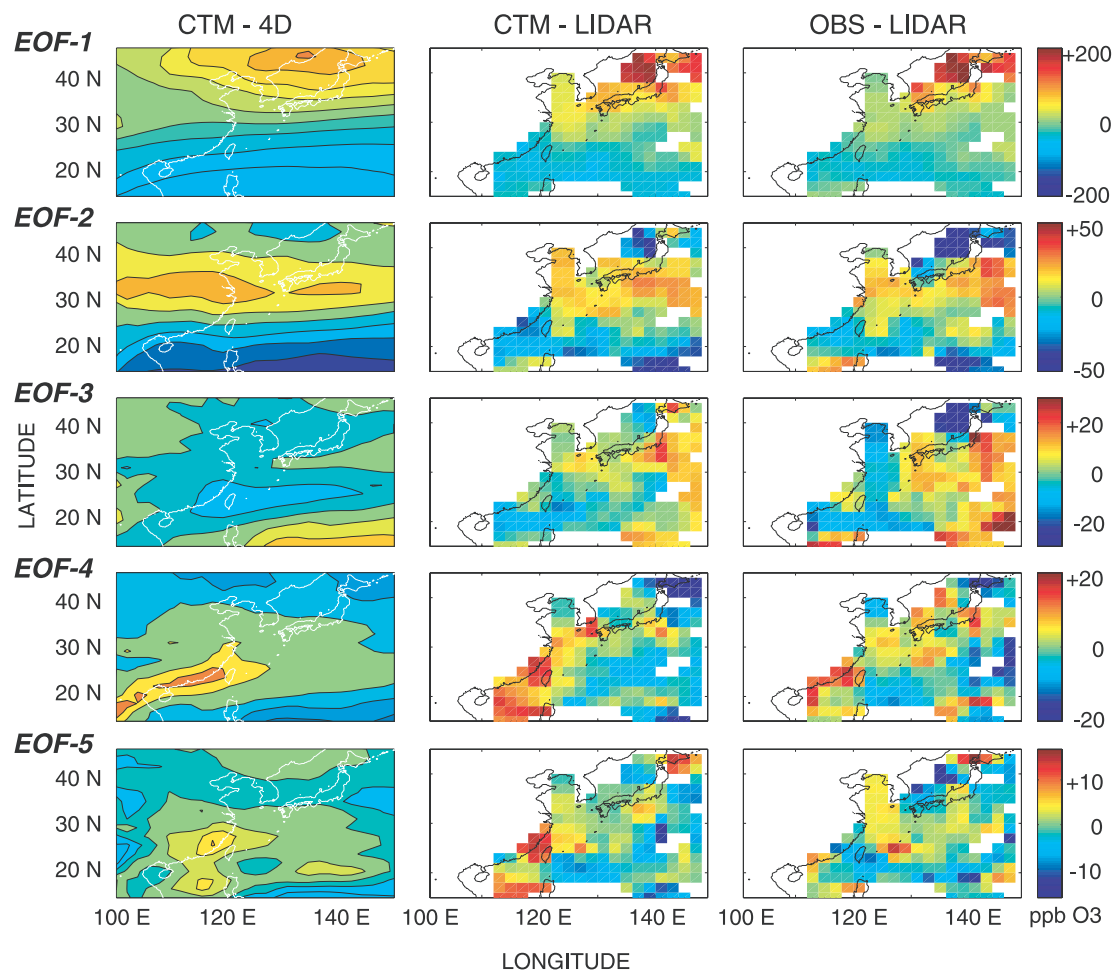


**Figure 8.** The time-averaged PCs (amplitudes of each EOF in ppb) obtained by projecting different centered data onto the EOF-1 to EOF-5 computed from the CTM 4-D data. The left panels show the PCs from the CTM 4-D data, the middle panels show the pseudo-PCs from the CTM simulation of the lidar, and the right panels show the pseudo-PCs from the lidar observations. For the lidar and simulated-lidar data here, the missing points are filled with the CTM simulated O<sub>3</sub> values.

agreement, and additional approaches to analyzing the lidar data for vertical structures are needed.

## 7. Conclusion

[41] We present a range of atypical statistical analyses of the TRACE-P observations of CO and O<sub>3</sub> to evaluate the representativeness of the TRACE-P observations and to provide possible new insights on the accuracy of chemistry-transport models. Representative is used here to mean that the data along the flight tracks has the same statistical properties as a uniform sampling of an extended region over eastern Asia and the western Pacific. This evaluation uses the modeled distributions from the FRSGC/UCI CTM driven by the Oslo T63L40 ECMWF forecast meteorology ( $1.9^\circ \times 1.9^\circ \times 500$  m) to compare flight track data with those from an extended 4-D domain defined arbitrarily as 14N to 46N, 100E to 150E, up to 18 km in height, and from 3 March to 3 April 2001. We assume the extended domain as providing unbiased statistics.

[42] We first focus on the central 50% of the distribution for CO and O<sub>3</sub>, since values can be thought of as

background air and generally avoid pollution plumes or stratospheric influences that appear at the extreme probabilities. For CO, outside of the boundary layer (0–1 km) and the region of dominant stratospheric influence (>10 km in midlatitudes), the 25th and 50th percentiles from the CTM along the flight tracks are basically the same as from the extended 4-D domain, and, moreover, these agree with the TRACE-P observations. In the boundary layer, the CTM flight tracks are systematically 10–20 ppb greater than the extended domain even though the domain includes continental emissions. This indicates that TRACE-P sampling is biased toward sampling pollution plumes. Furthermore, both CTM extended domain and flight tracks are less than the observations, particularly so for the tropical region. Thus the cumulative probability functions for CO support the generally excellent CTM simulation of the observations but for a systematic underestimate of nearby emissions. Even the frequency of low-CO stratospheric influence is well matched along flight tracks but is atypical of the extended domain. For O<sub>3</sub> these same probability functions clearly point out problems: excessive boundary-layer production in midlatitudes but a missing source in the tropics.

[43] The 10th, 50th, and 90th percentiles of the latitude-by-height distribution of lidar  $O_3$  show how the CTM reproduces the nonrepresentative clumpy nature of the observations, which is dramatically different than the smooth patterns from the extended domain even at the extreme (10th and 90th) percentiles. This model-measurement comparison also shows good agreement for the statistical height of the stratosphere-troposphere transition (defined here as 100 ppb  $O_3$ ), except about the jet region (30–35N) where the model shows intrusion of the 100-ppb air to much lower heights.

[44] Adaptive kernel estimation of the 2-D probability density of  $O_3$ -CO correlations shows a very good simulation of two different chemical regimes (stratospheric and polluted) that is quite different from the extended domain. It also clearly points out the model failure to predict CO > 400 ppb. For the EOF analysis of the vertical  $O_3$  profiles, the lidar curtain sampling along the flight tracks has the EOF structures shifted downward about 1 km as compared with the extended domain. The latitude-by-longitude maps of the principal components show larger amplitudes for the CTM flight tracks as compared with the extended CTM domain indicating inadequate sampling or bias toward sampling anomalous events. In summary, for most tests we find that the TRACE-P data set shows some statistical biases in sampling and cannot be simply taken as representative of the chemistry and ozone distributions over eastern Asia and the western Pacific in March 2001.

[45] In evaluating model error using these new statistical measures, we find that the FRSGC/UCI CTM simulation of the TRACE-P flight-track data is in most cases quite good and is even better when one takes into account the biased sampling of the extended domain by the specific flight tracks. For example, the CTM does an excellent job in simulating the stratospheric influence in the upper troposphere for the TRACE-P flights, and this influence is quite different from that averaged over the larger region. In previously noted cases in which the model failed to match high-CO events or produced too high  $O_3$  abundances in the boundary layer, these new analyses point out that the errors are most likely due to source-region errors (e.g., CO emissions or near-field  $O_3$  production) rather than meteorological errors. In most cases the modeled flight-track data look much more like the observations than the model averaged over the region, indicating that the specific spatial and meteorological characteristics of the observations are captured.

[46] Overall, the TRACE-P sampling is not representative of the larger domain we selected. Similar results would likely apply for any useful domain size. We believe that the simplest explanation for this is a combination of the limited number of observations plus TRACE-P strategy of sampling the chemical processes in pollution plumes leaving Asia and stratospheric intrusion events associated with cyclones. If one uses such campaign data to detect systematic long-term changes (e.g., between overlapping campaigns such as TRACE-P and PEM-West B [Davis et al., 2003]) or to provide long-term calibration for satellite observations, then the representativeness of the different data sets needs to be evaluated.

[47] **Acknowledgments.** This work was supported by the NASA Tropospheric Chemistry Program part of the TRACE-P mission.

## References

- Baldwin, M. P., and T. J. Dunkerton (1999), Propagation of the Arctic Oscillation from the stratosphere to the troposphere, *J. Geophys. Res.*, **104**, 30,937–30,946.
- Browell, E. V., et al. (2003), Large-scale ozone and aerosol distributions, air mass characteristics, and ozone fluxes over the western Pacific Ocean in late winter/early spring, *J. Geophys. Res.*, **108**(D20), 8805, doi:10.1029/2002JD003290.
- Carmichael, G., et al. (2003), Regional-scale chemical transport modeling in support of intensive field experiments: Overview and analysis of the TRACE-P observations, *J. Geophys. Res.*, **108**(D21), 8823, doi:10.1029/2002JD003117.
- Conway, T. J., P. P. Tans, L. S. Waterman, and K. W. Thoning (1994), Evidence for interannual variability of the carbon cycle from the National Oceanic and Atmospheric Administration Climate Monitoring and Diagnostics Laboratory Global Air Sampling Network, *J. Geophys. Res.*, **99**(D11), 22,831–22,855.
- Corti, S., F. Molteni, and T. N. Palmer (1999), Signature of climate change in atmospheric circulation regime frequencies, *Nature*, **398**, 799–802.
- Davis, D. D., et al. (2003), Trends in western North Pacific ozone photochemistry as defined by observations from NASA's PEM-West B [1994] and TRACE-P [2001] field studies, *J. Geophys. Res.*, **108**(D21), 8829, doi:10.1029/2002JD003232.
- Dlugokencky, E. J., K. A. Masarie, P. M. Lang, P. P. Tans, L. P. Steele, and E. G. Nisbet (1994), A dramatic decrease in the growth rate of atmospheric methane in the Northern Hemisphere during 1992, *Geophys. Res. Lett.*, **21**(1), 45–48.
- Dommenget, D., and M. Latif (2002), A cautionary note on the interpretation of EOFs, *J. Clim.*, **15**, 216–225.
- Gallardo, L., J. Carrasco, and G. Olivares (2000), An analysis of ozone measurements at Cerro Tololo (30 degrees S, 70 degrees W, 2200 m.a.s.l.) in Chile, *Tellus, Ser. B*, **52**(1), 50–59.
- Haszpra, L. (1999), On the representativeness of carbon dioxide measurements, *J. Geophys. Res.*, **104**(D21), 26,953–26,960.
- Hsu, C. J., and F. Zwiers (2001), Climate change in recurrent regimes and modes of Northern Hemisphere atmospheric variability, *J. Geophys. Res.*, **106**, 20,145–20,159.
- Inoue, H. Y., and H. Masueda (2001), Measurements of atmospheric CO<sub>2</sub> from a meteorological tower in Tsukuba, Japan, *Tellus, Ser. B*, **53**(3), 205–219.
- Jacob, D. J., J. Crawford, M. M. Kleb, V. S. Connors, R. J. Bendura, J. L. Raper, G. W. Sachse, J. Gille, L. Emmons, and J. C. Heald (2003), The Transport and Chemical Evolution over the Pacific (TRACE-P) aircraft mission: Design, execution and first results, *J. Geophys. Res.*, **108**(D20), 8781, doi:10.1029/2002JD003276.
- Kiley, C., et al. (2003), An intercomparison and evaluation of aircraft-derived and simulated CO from seven chemical transport models during the TRACE-P experiment, *J. Geophys. Res.*, **108**(D21), 8819, doi:10.1029/2002JD003089.
- Kimoto, M., and M. Ghil (1993), Multiple flow regimes in the northern Hemispheric winter, part I: Methodology and hemispheric regimes, *J. Atmos. Sci.*, **50**, 2625–2643.
- Liu, H. Y., D. J. Jacob, I. Bey, R. M. Yantosca, B. N. Duncan, and G. W. Sachse (2003), Transport pathways for Asian combustion outflow over the Pacific: Interannual and seasonal variations, *J. Geophys. Res.*, **108**(D2), 8786, doi:10.1029/2002JD003102.
- Lorenz, E. N. (1956), Empirical Orthogonal Functions and statistical weather predictions, *Sci. Rep. I*, 49 pp., Dept. of Meteorol., Mass. Inst. of Tech., Cambridge, Mass.
- Martin, R. V., D. J. Jacob, J. A. Logan, J. R. Ziemke, and R. Washington (2000), Detection of a lightning influence on tropical tropospheric ozone using empirical orthogonal functions, *Geophys. Res. Lett.*, **27**, 1639–1642.
- McLinden, C. A., S. Olsen, B. Hannegan, O. Wild, M. J. Prather, and J. Sundet (2000), Stratospheric ozone in 3-D models: A simple chemistry and the cross-tropopause flux, *J. Geophys. Res.*, **105**, 14,653–14,665.
- Navascues, B., and C. Rus (1991), Carbon-dioxide observations at Izaña-baseline-station, Tenerife (Canary-Islands)-1984–1988, *Tellus, Ser. B*, **43**(2), 118–125.
- Palmer, P. I., D. J. Jacob, D. B. A. Jones, C. L. Heald, R. M. Yantosca, J. A. Logan, G. W. Sachse, and D. G. Streets (2003), Inverting for emissions of carbon monoxide from Asia using aircraft observations over the western Pacific, *J. Geophys. Res.*, **108**(D21), 8828, doi:10.1029/2003JD003397.
- Parrish, D. D., J. S. Holloway, M. Trainer, P. C. Murphy, G. L. Forbes, and F. C. Fehsenfeld (1993), Export of North American ozone pollution to the North Atlantic Ocean, *Science*, **259**, 1436–1439.
- Parrish, D. D., M. Trainer, J. S. Holloway, J. E. Yee, M. S. Warshawsky, F. C. Fehsenfeld, G. L. Forbes, and J. L. Moody (1998), Relationships between ozone and carbon monoxide at surface sites in the North Atlantic region, *J. Geophys. Res.*, **103**, 13,357–13,376.

- Pierce, R. B., et al. (2003), Regional Air Quality Modeling System (RAQMS) predictions of the tropospheric ozone budget over east Asia, *J. Geophys. Res.*, **108**(D21), 8825, doi:10.1029/2002JD003397.
- Russo, R. S., et al. (2003), Chemical composition of Asian continental outflow over the western Pacific: Results from TRACE-P, *J. Geophys. Res.*, **108**(D2), 8804, doi:10.1029/2002JD003184.
- Silverman, B.W. (1986), *Density Estimation for Statistics and Data Analysis*, 175 pp., Chapman and Hall, New York.
- Simpson, I. J., N. J. Blake, D. R. Blake, E. Atlas, F. Flocke, J. H. Crawford, H. E. Fuelberg, C. M. Kiley, S. Meinardi, and F. S. Rowland (2003), Photochemical production and evolution of selected C<sub>2</sub>–C<sub>5</sub> alkyl nitrates in tropospheric air influenced by Asian outflow, *J. Geophys. Res.*, **108**(D20), 8808, doi:10.1029/2002JD002830.
- Talbot, R. W., et al. (2003), Reactive nitrogen in Asian Continental Outflow over the western Pacific: Results from the NASA TRACE-P airborne mission, *J. Geophys. Res.*, **108**(D2), 8803, doi:10.1029/2002JD003129.
- Thompson, D. W. J., and J. M. Wallace (1998), The Arctic Oscillation signature in the wintertime geopotential height and temperature fields, *Geophys. Res. Lett.*, **25**, 1297–1300.
- Thompson, D. W. J., and J. M. Wallace (2000), Annular modes in the extratropical circulation. part I: Month-to-month variability, *J. Clim.*, **13**, 1000–1016.
- Wild, O., and M. J. Prather (2000), Excitation of the primary tropospheric chemical mode in a global 3-D model, *J. Geophys. Res.*, **105**, 24,647–24,660.
- Wild, O., J. K. Sundet, M. J. Prather, I. S. A. Isaksen, H. Akimoto, E. V. Browell, and S. J. Oltmans (2003), CTM ozone simulations for spring 2001 over the western Pacific: Comparisons with TRACE-P lidar, ozone-sondes, and TOMS columns, *J. Geophys. Res.*, **108**(D21), 8826, doi:10.1029/2002JD003283.
- Wilks, D. S. (1995), *Statistical Methods in the Atmospheric Sciences*, 467 pp., Academic, San Diego, Calif.
- M. A. Avery, E. V. Browell, and G. W. Sachse, Atmospheric Sciences Competency, NASA Langley Research Center, Hampton, VA 23681-0001, USA. (m.a.avery@larc.nasa.gov; edward.v.browell@nasa.gov; glen.w.sachse@nasa.gov)
- J. Hsu and M. J. Prather, Department of Earth System Science, University of California, Irvine, 2101 Croul Hall, Irvine, CA 92697, USA. (juno@halo.ps.uci.edu; mprather@uci.edu)
- I. S. A. Isaksen and J. K. Sundet, Department of Geophysics, University of Oslo, Box 1022, 0315 Oslo, Norway. (ivar.isaksen@geo.uio.no; j.k.sundet@geofysikk.uio.no)
- O. Wild, Frontier Research System for Global Change, 3173-25 Showa-machi, Yokohama, Kanagawa 236-0001, Japan. (oliver@jamstec.go.jp)